

# A fiber orientation-adapted integration scheme for computing the hyperelastic Tucker average for short fiber reinforced composites

Niels Goldberg<sup>1</sup> · Felix Ospald<sup>2</sup> · Matti Schneider<sup>3</sup>

Received: 13 October 2016 / Accepted: 22 May 2017 / Published online: 7 June 2017  
© Springer-Verlag Berlin Heidelberg 2017

**Abstract** In this article we introduce a fiber orientation-adapted integration scheme for Tucker’s orientation averaging procedure applied to non-linear material laws, based on angular central Gaussian fiber orientation distributions. This method is stable w.r.t. fiber orientations degenerating into planar states and enables the construction of orthotropic hyperelastic energies for truly orthotropic fiber orientation states. We establish a reference scenario for fitting the Tucker average of a transversely isotropic hyperelastic energy, corresponding to a uni-directional fiber orientation, to microstructural simulations, obtained by FFT-based computational homogenization of neo-Hookean constituents. We carefully discuss ideas for accelerating the identification process, leading to a tremendous speed-up compared to a naive approach. The resulting hyperelastic material map turns out to be surprisingly accurate, simple to integrate in commercial finite element codes and fast in its execution. We demonstrate the capabilities of the extracted model by a finite element analysis of a fiber reinforced chain link.

**Keywords** Computational homogenization · Hyperelasticity · Short fibers · Composite materials ·

Orientation tensors · Numerical integration · Injection molding

## 1 Introduction

The primary obstacle for the derivation of simple homogenization formulae for the effective inelastic or hyperelastic behavior of fiber reinforced composites is the lack of useful analytical solutions. This situation contrasts with the linear elastic case, where Eshelby’s solution [10, 11] for a single ellipsoidal inhomogeneity in a homogeneous matrix serves as the basis for a variety of extremely powerful and predictive mean-field homogenization techniques [8, 22, 39, 59].

To overcome this lack of analytical solutions, two main ideas emerged. On the one hand, resorting to linear comparison principles, see Ponte-Castañeda and Suquet [48] for an overview, yields insight into the structure of effective material properties. On the other hand, the importance of numerical solution methods for characterizing the effective nonlinear behavior of composites cannot be underestimated. Almost all approaches for such a characterization are based on computational techniques, ranging from calculations for rather simple structures substituting Eshelby’s explicit solution to full-field microstructural simulations resolving the full microstructural features.

One of the former techniques is Doghri’s method of pseudo-grains [29], where the response of the uni-directional fiber orientation state is subsequently averaged to account for distributed fiber orientations. The approach is rather general, and can be applied to a variety of inelastic material behavior. Similar considerations were carried out by Li et al. [32], based on Miehe’s microsphere method [36].

There is a vast literature on full-field microstructural solvers, among them finite element [20], finite differ-

✉ Niels Goldberg  
niels.goldberg@mb.tu-chemnitz.de

Felix Ospald  
felix.ospald@mathematik.tu-chemnitz.de

Matti Schneider  
matti.schneider@itwm.fraunhofer.de

<sup>1</sup> TU Chemnitz, Professur Festkörpermechanik, Chemnitz, Germany

<sup>2</sup> TU Chemnitz, Professur Numerische Mathematik (PDE), Chemnitz, Germany

<sup>3</sup> Fraunhofer ITWM, Kaiserslautern, Germany

ence [51], finite volume [4] and pseudospectral methods [42]. With the help of these solvers access to all microstructural features can be gained. However, all of them demand computational resources exceeding the computational resources necessary for conventional finite element simulations on the macro scale, see for instance Mosby-Matouš [40].

To alleviate the computational burden of full field simulations, model order reduction techniques [34,35] for computing effective inelastic properties are gaining popularity. Also, full field simulations are used as a replacement for experiments whose results are subsequently fitted to pre-defined anisotropic material models. Indeed, conducting experiments for a prescribed fiber orientation state excluding boundary effects for complex loading scenarios like shearing can be challenging. Instead, characterizing the (often isotropic) material behavior of the constituents and subsequently accounting for small process-induced alterations of the materials' characteristics by simple tensile tests appears to be a practical solution.

This work is focussed on the latter scenario: in the context of hyperelasticity we generate deformation-stress pairs for a variety of fiber orientation tensors and prescribed loading scenarios with the help of the FFT-based computational method of Moulinec-Suquet [42]. Then, we fit the obtained data to some pre-defined material model explicitly taking into account the fiber orientation states.

At first glance, this work shares many similarities with Li et al. [32], Kammoun et al. [29] or Yvonnet et al. [58]. Our key contribution is a method for obtaining an anisotropic material model from a transversely isotropic model, explicitly taking into account the fiber orientation, with very beneficial structural properties. Averaging transversely isotropic hyperelastic energies has been considered before, for instance in the work of Miehe [36], Kammoun et al. [29] or Li et al. [32]. Miehe restricts to an isotropic distribution of directions. Taking into account distributed directions, as for fiber orientation distribution functions, introduces an additional difficulty: the fiber orientation states can degenerate to two-dimensional distributions. Hence, a fixed number of Gauss points on the sphere cannot integrate such functions with sufficient accuracy, see for instance Li et al. [32], who states that not even 600 Gauss points yield sufficient accuracy. That would not be a problem if these two-dimensional states were infrequent. However, quite the opposite is the case. In particular for thin-walled structures the occurring fiber orientation states are almost exclusively close to planar.

To overcome these limitations we take a closer look at the modelling of fiber orientations and their evolution during injection molding. A particular class of fiber orientation distribution functions, called angular central Gaussian distributions [54], plays a dominant role for injection mold-

ing simulations, as they constitute an exact solution for a simplified model of fiber orientation dynamics [47], in particular in terms of the so-called (fast) exact closure [38]. Angular central Gaussian distributions have the nice property that they can be obtained from an isotropic distribution on the sphere by a global transformation. This observation, which also forms the basis of fiber-filled volume element structure generators, see Ospald-Herzog [21], can be used for our problem. Given a set of Gauss points on the sphere, tailored for the isotropic distribution, fiber orientation distribution adapted Gauss points can be obtained by applying the previously mentioned global transformation to the original Gauss points. Using this idea, rotations and degenerations of the fiber orientation are easily taken care of, preserving symmetries and requiring only very few Gauss points compared to previous work [32].

The nonlinear version of Tucker's averaging procedure [5] preserves structural properties of the transversely isotropic hyperelastic energy density and the fiber orientation distribution in the sense that convexity properties of the energy density are inherited, as well as symmetry properties of the orientation distribution. At this point it should be mentioned that writing down, for instance, a fully orthotropic quasiconvex hyperelastic energy density with good approximation properties by hand is difficult, see Schröder-Neff [53].

The invariant-based hyperelastic energy for unidirectional discontinuously reinforced composites introduced in Goldberg et al. [18] serves as our starting point. In contrast to Kammoun et al. [29] we do not use this energy for homogenization, i.e. one first identifies the material parameters and subsequently averages. Instead, we rely upon an a posteriori strategy, i.e. we leave the parameters of the transversely isotropic model free and fit the averaged model to the microstructure simulation data. This idea, albeit simple, reduces the average relative stress error by a factor of two compared to the a priori approach, at least for the computational example in this work (polypropylene reinforced with 20 vol-% glass fibers).

This article is organized as follows. Section 2 discusses homogenization at finite strains briefly. Then, in Sect. 3, the structural properties of Tucker's averaging procedure are discussed and specialized to the angular central Gaussian distribution. We detail on the identification strategy for the effective model in Sect. 4, discussing the different fiber orientation states, FFT-based computational homogenization and the used transversely isotropic model. Last but not least we identify a material model for glass fiber reinforced polypropylene, compare its results to approaches in the literature, study the sensitivity to reducing the number of necessary precomputations and apply it to the large deformation of a fiber reinforced chain link.

## 2 Homogenization at finite strains

Let  $Y = [0, L_1] \times [0, L_2] \times [0, L_3]$  be a volume with dimensions  $L_1, L_2$  as well as  $L_3$  and let  $K$  materials ( $k = 1, \dots, K$ ) with hyperelastic energy functions  $W_k$  be given, defined on disjoint subsets  $\Omega_k \subset Y$  whose closure covers  $Y$ . According to Hill [23], the effective hyperelastic energy  $\bar{W}$  to the prescribed deformation gradient  $\bar{F} \in \mathbb{R}^{3 \times 3}$  with  $\det \bar{F} > 0$  computes from the multi-cell homogenization problem [17,43]

$$\bar{W}(\bar{F}) = \inf_{n \geq 1} \inf \left\{ \frac{1}{|nY|} \int_{nY} W(X, F) dX \mid \begin{array}{l} u : nY \rightarrow \mathbb{R}^3 \text{ periodic, } \\ F = \bar{F} + \nabla u, \end{array} \right. \quad (2.1)$$

where  $W(X, F) = \sum_{k=1}^K \chi_{\Omega_k}(X) W_k(F)$ ,  $\chi_S$  denotes the characteristic function of the set  $S$  and  $W$  is extended  $(L_1, L_2, L_3)$ -periodically. In contrast to homogenization at small strains, compare Miehe-Koch [37], it might be insufficient to work on the original cell  $Y$ . Due to the non-convexity of the hyperelastic energy  $W$ , in addition to the local displacement fluctuation  $u$  the critical number of unit cells  $n$  needs to be determined. A typical procedure would be to start at  $n = 1$  and to subsequently increase  $n$  until the effective energy does not change by increasing  $n$  further. In general, the number  $n$  and the corresponding ensemble of cells  $nY$  depend on the macroscopic deformation gradient  $\bar{F}$ , see Schröder [52].

The formal Euler-Lagrange equation associated to the homogenization problem (2.1) reads

$$\text{Div}(P) = 0, \quad (2.2)$$

where  $P = \frac{\partial W}{\partial F}$  denotes the first Piola-Kirchhoff stress tensor, and  $\text{Div}$  refers to the (weak) right divergence, i.e.  $\text{Div}(P)_i = \partial_j P_{ij}$  in Cartesian coordinates. Once the displacement fluctuation  $u : nY \rightarrow \mathbb{R}^3$  is determined, the effective first Piola-Kirchhoff stress is computed by volume averaging

$$\bar{P} = \frac{1}{|nY|} \int_{nY} P(X, \bar{F} + \nabla u) dX.$$

We will also use the short hand notation  $\langle P \rangle_{nY}$  for the latter average. The effective first Piola-Kirchhoff stress is related to the effective hyperelastic energy by the usual relation  $\bar{P} = \frac{\partial \bar{W}}{\partial \bar{F}}$ , see Hill [23]. Notice that not every stress measure at finite strains can be consistently averaged. Apart from the first Piola Kirchhoff stress also the Cauchy stress can be averaged

$$\bar{\sigma} = \langle \sigma \rangle,$$

where the latter average is carried out on the deformed element, s.t. the relation  $\bar{\sigma} = \det(\bar{F})^{-1} \bar{P} \bar{F}^T$  holds.

For moderate deformations it is believed that only a single cell  $Y$ , i.e.  $n = 1$  is sufficient, see Neukamm-Schäffner

[45] for a theoretical investigation. We will rely upon this hypothesis throughout this work.

## 3 Tucker averaging and the structure of an effective model

### 3.1 Tucker’s orientation averaging at finite strains

Advani-Tucker [5] suggested a procedure to obtain the effective linear elastic stress of a fiber reinforced composite from knowledge of the fiber orientation distribution function  $\psi$  and the effective elastic tensor corresponding to an aligned fiber orientation state. In this linear elastic context, the fiber orientation distribution enters into the effective elastic tensor only through the second and fourth order orientation tensors

$$A = \int_{S^2} (p \otimes p) \psi(p) dS(p) \quad \text{and} \\ \mathbb{A} = \int_{S^2} (p \otimes p \otimes p \otimes p) \psi(p) dS(p),$$

where  $dS$  denotes the standard surface measure on the sphere  $S^2 \subseteq \mathbb{R}^3$  and the fiber directions  $\{p\}$  are measured in the Lagrangian configuration. From a mechanical point of view, this averaging procedure can be interpreted as a variant of Voigt’s upper bound [55], a very simple formula for obtaining an estimate for the effective elastic response. The advantage of Advani-Tucker’s procedure comes from its simplicity, together with its beneficial structural properties (see below). However, as already mentioned, this averaging gives rise to an upper bound and thus overestimates the stiffness of the composites, see Sec. 5.4 for a discussion.

We generalize Tucker’s averaging procedure to the setting of hyperelasticity as follows. Suppose a fiber orientation distribution function  $\psi$  is given, together with a family  $\{W(\cdot, p)\}_{p \in P}$  of hyperelastic stored energy functions. Each  $W(\cdot, p) : F \mapsto W(F, p)$  is parametrized by a direction  $p \in S^2$  and constitutes an effective hyperelastic energy for the fiber orientation state aligned in direction  $p$ . For reasons of frame independence, this family of energies satisfies the consistency condition

$$W(F, Qp) = W(Q^T F, p), \quad F \in \mathbb{R}^{3 \times 3}, \quad \det F > 0, \\ Q \in \mathbb{R}^{3 \times 3}, \quad Q^T Q = \text{Id}, \quad \det Q = 1, \quad (3.1)$$

which says that if we apply the same orthogonal transformation to the microstructure and the applied load, the stored energy of this transformed configuration coincides with the energy of the original configuration. Then, the corresponding orientation-averaged stored energy function is defined via

$$\begin{aligned}\bar{W}^{AT}(F) &= \int_{S^2} W(F, p) \psi(p) dS(p), \\ F &\in \mathbb{R}^{3 \times 3}, \quad \det F > 0,\end{aligned}\quad (3.2)$$

where the superscript  $AT$  stands for Advani-Tucker. The probability density function  $\psi$  is non-negative and integrates to 1. Thus, (3.2) represents a convex combination of energy densities. In particular, properties like rank-one-, poly- and quasiconvexity are inherited from the particulate energy densities  $\{W(\cdot, p)\}_{p \in P}$ . Furthermore, if the fiber orientation distribution function  $\psi$  possesses a particular sample symmetry, this symmetry is inherited by the Advani-Tucker average  $\bar{W}^{AT}$ . Indeed, suppose that  $\psi(Qp) = \psi(p)$  for all  $p \in S^2$  and a fixed matrix  $Q \in \mathbb{R}^{3 \times 3}$ ,  $\det Q > 0$ . Then, invoking (3.1), we see for every  $F$

$$\begin{aligned}\bar{W}^{AT}(Q^T F) &= \int_{S^2} W(Q^T F, p) \psi(p) dS(p) \\ &= \int_{S^2} W(F, Qp) \psi(p) dS(p) \quad (q := Qp) \\ &= \det Q \int_{S^2} W(F, q) \psi(Q^T q) dS(q) \\ &= \det Q \int_{S^2} W(F, q) \psi(q) dS(q) \\ &= \det Q \bar{W}^{AT}(F).\end{aligned}$$

The prefactor  $\det Q$  vanishes if  $Q$  is an orthogonal transformation. In particular, averaging the isotropic fiber orientation  $\psi \equiv \frac{1}{4\pi}$  always leads to an isotropic orientation average  $\bar{W}^{AT}$ . Also, an orthotropic  $\psi$  yields an orthotropic  $\bar{W}^{AT}$  with the same axes of orthotropy.

We consider the latter two key structural properties to be particularly powerful for constructing an effective hyperelastic energy for short fiber reinforced composites.

From the definition of relation (3.2) we see that the large deformation stress measures also arise from an orientation averaging procedure. In contrast to the (exact) homogenization of Sect. 2 also the second Piola-Kirchhoff stress  $S$ , which arises as the derivative of the hyperelastic energy with respect to the right Cauchy-Green tensor  $C = F^T F$ , can be averaged. As differentiation commutes with integration one obtains

$$\begin{aligned}\bar{S}^{AT}(F) &= \int_{S^2} \psi(p) S(F, p) dS(p) \\ &= \int_{S^2} \psi(p) 2 \frac{\partial W}{\partial C}(F, p) dS(p) \\ &= 2 \frac{\partial}{\partial C} \int_{S^2} \psi(p) W(F, p) dS(p) = 2 \frac{\partial \bar{W}^{AT}}{\partial C}(F),\end{aligned}$$

where we utilized the definition

$$S(F, p) = 2 \frac{\partial W(F, p)}{\partial C}.$$

For notational simplicity and if no confusion arises we occasionally consider the second Piola-Kirchhoff stress tensor  $S$  and the energy  $W$  as functions of the right Cauchy-Green tensor.

### 3.2 The angular central Gaussian distribution and efficient integration

In principle, any fiber orientation distribution  $\psi$  leads to the beneficial structural properties advertized in Sect. 3.1. However, there are two distinct constraining factors for choosing  $\psi$ . On the one hand,  $\psi$  should accurately represent the occurring fiber orientation in a fiber reinforced composite structure. On the other hand,  $\psi$  should enable efficient handling, in particular in terms of carrying out the integration (3.2).

A class of fiber distributions satisfying both of these requirements is given by the three dimensional angular central Gaussian (ACG) distributions, see Tyler [54] for a discussion from the statistician's point of view. These distributions are parameterised by a symmetric and positive definite  $3 \times 3$  matrix  $B$  with determinant one, and defined by

$$\psi_B(p) = \frac{1}{4\pi} (p^T B p)^{-\frac{3}{2}}, \quad p \in S^2. \quad (3.3)$$

It can be shown, see [9,33], that these functions  $\psi_B(t)$  constitute exact solutions to Jeffery's equation [24], which governs the dynamics of a single ellipsoidal fiber in shear flow. In particular, working with these distributions can be extremely advantageous for injection molding simulations, see Montgomery-Smith and co-workers [38].

In most practical applications, the local fiber orientation is described by the fiber orientation tensor  $A$  of second order. Montgomery-Smith et al. [38] show that there is a one-to-one correspondence between parameters  $B$  for the angular central Gaussian distribution (3.3), i.e. positive definite  $3 \times 3$  matrices  $B$  with determinant one, and non-degenerated fiber orientation tensors of second order, i.e. positive definite  $3 \times 3$  matrices  $A$  with trace one, connected by the defining relationship

$$A = \int_{S^2} p \otimes p \psi_B(p) dS(p).$$

Montgomery-Smith et al. [38] discuss the efficient computation of the latter integral.

There is another striking advantage of the ACG distributions, namely in terms of numerical integration on the sphere. In the context of ACG the general averaging formula (3.2) takes the form

$$\begin{aligned}W_B(F) &= \frac{1}{4\pi} \int_{S^2} (p^T B p)^{-\frac{3}{2}} W(F, p) dS(p), \\ F &\in \mathbb{R}^{3 \times 3}, \quad \det F > 0.\end{aligned}\quad (3.4)$$

Due to the strong nonlinearity of the stored energy functions  $W(\cdot, p)$  arising in hyperelasticity this integral needs to be evaluated by numerical means in practice. However, conventional Gaussian quadrature schemes on the sphere (cf. [7, 19, 31]) appear to be unsuited, as the fiber orientation density can be strongly localized. For instance, if the second order orientation tensor has rank one  $A = p \otimes p$ , then only the Dirac distribution  $\frac{1}{2}(\delta_p + \delta_{-p})$  realizes  $A$ . Also, if  $A$  is close to  $p \otimes p$ , the corresponding fiber orientation distribution function is strongly localized around the points  $p$  and  $-p$ . To circumvent these problems, we make use of the transformation of variables formula

$$\int_{S^2} \psi_B(p)W(F, p) dS(p) = \frac{1}{4\pi} \int_{S^2} W(F, t(p)) dS(p)$$

with the transformation  $t(p) = \frac{B^{-\frac{1}{2}}p}{\|B^{-\frac{1}{2}}p\|}$ , (3.5)

valid for any function  $W$  on the sphere. Formula (3.5) converts any ACG density  $\psi_B$  to a uniform distribution, transferring the distribution data into the evaluation of the function  $W$  via the transformation  $t$ . The change of variable rule (3.5) is implicit in previous work, like in Dinh-Armstrong [9]. We provide a self-contained derivation in Appendix A. For the transformed problem, standard quadrature rules on the sphere can be applied, i.e.

$$\int_{S^2} \psi_B(p)W(F, p) dS(p) \approx \sum_{i=1}^N w_i W(F, t(p_i)), \quad (3.6)$$

where  $\{p_i\}_{i=1}^N$  is a set of quadrature points on the sphere, and  $w_i > 0$  are the corresponding positive quadrature weights with  $\sum_{i=1}^N w_i = 1$ .

Figure 1 visualizes the transformed Gauss points for different orientations. The untransformed points are represented by 210 uniformly distributed points  $\{p_i\}$  on a hemisphere of  $S^2$  as shown in Fig. 1a. The remaining figures show examples of the transformed points  $\{t(p_i)\}$  for different ACG distribution parameters  $B$ , calculated from the fiber orientation tensor  $A$  of second order. The transformed Gauss points adapt accurately to the features of the corresponding ACG fiber orientation distributions.

### 4 Identification of the effective model

We wish to identify an effective hyperelastic model for short fiber reinforced composites, taking into account both the local fiber orientation state and the applied deformation. For that purpose, in a first step we generate training data by microstructural simulations. More precisely, we identify independent fiber orientation states and sample points uniformly in the resulting configuration space. Then, we

determine a number of test deformations, whose hyperelastic effective stress is computed, for each pre-identified fiber orientation state, by FFT-based computational homogenization.

In a second step we introduce a robust transversely isotropic stored energy function, depending on a number of parameters  $\alpha$ . The orientation averaging procedure of Sect. 3.1 gives rise to a family of stored energy functions, depending on the fiber orientation state and yet undetermined parameters  $\alpha$ . In the final step we use a least squares method to find those parameters which fit the training data best.

#### 4.1 Essentially different fiber orientations and their generation

In commercial injection molding software [1–3], the local fiber orientation state is described by the fiber orientation tensor  $A$  of second order, determined from a finite set of directions  $\{p_1, \dots, p_N\}$  by the formula

$$A = \frac{1}{N} \sum_{i=1}^N p_i \otimes p_i.$$

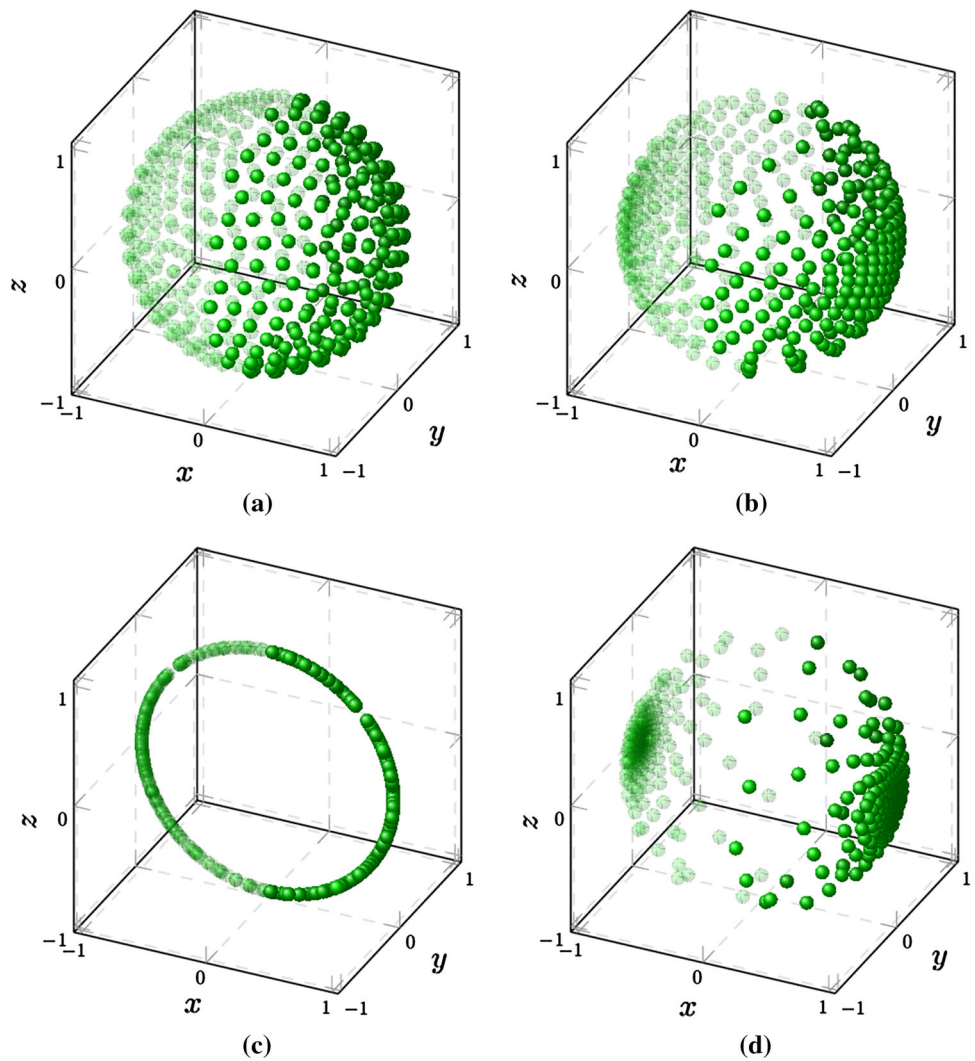
Thus,  $A$  is a symmetric and positive semidefinite  $3 \times 3$  matrix. Suppose, for each such fiber orientation state  $A$  we have an effective hyperelastic stored energy function  $W_A$ . By material objectivity, simultaneously changing the frame for  $A$  and the deformation  $F$  preserves the stored energy. Translated into mathematical terms this amounts to the identity  $W_A(Q^T F) = W(F, QAQ^T)$  for any second order fiber orientation tensor  $A$ , deformation gradient  $F$  and orthogonal transformation  $Q$ . The latter consistency condition can also be read in reverse. As any fiber orientation tensor  $A$  admits an eigenvalue decomposition  $A = U \Lambda U^T$  with orthogonal  $U$  and diagonal  $\Lambda = \text{diag}(\lambda_1, \lambda_2, \lambda_3)$  with  $\lambda_1 \geq \lambda_2 \geq \lambda_3$ , it suffices to construct stored energy functions for diagonal fiber orientation tensors. Taking into account the normalization  $\text{tr}(A) = 1$ , which translates into  $\lambda_1 + \lambda_2 + \lambda_3 = 1$ , it suffices to consider a two-dimensional configuration space instead of the six- (or five-)dimensional space of all fiber orientations, reducing the computational complexity significantly.

To generate training data for the current investigation, in addition to the fiber orientation, prescribed loading scenarios are required. We chose four different loading scenarios, corresponding to uniaxial, planar and volumetric extension as well as a shear load case. These deformation scenarios are illustrated in Fig. 3a–d, and the corresponding mixed boundary conditions are listed in Table 1.

#### 4.2 FFT-based computational homogenization

For the computation of the hyperelastic response of the prescribed deformation scenarios on the various volume ele-

**Fig. 1** Visualization of (transformed) integration points for some second order fiber orientation tensors  $A$  and  $B$ -tensor. Only half of the points (with  $x \geq 0$ ) are actually used, due to the symmetry  $\psi_B(p) = \psi_B(-p)$ . **a**  $A = \text{diag}(\frac{1}{3}, \frac{1}{3}, \frac{1}{3})$ ,  $B = \text{diag}(1, 1, 1)$ . **b**  $A = \text{diag}(\frac{1}{2}, \frac{1}{3}, \frac{1}{6})$ ,  $B \approx \text{diag}(0.430, 0.891, 2.61)$  **c**  $A = \text{diag}(\frac{2}{3}, 0, \frac{1}{3})$ ,  $B \rightarrow \text{diag}(0, \infty, 0)$ ,  $\frac{B_{33}}{B_{11}} \rightarrow 2\frac{1}{3}$ . **d**  $A = \text{diag}(\frac{5}{6}, \frac{1}{12}, \frac{1}{12})$ ,  $B \approx \text{diag}(0.0611, 4.05, 4.05)$



ments we use the FFT-based computational homogenization method of Moulinec-Suquet [41, 42], extended to the hyperelastic setting in Lahellec et al. [30]. In this context, the governing differential equation (2.2) is discretized on a regular Cartesian grid using a discretization by trigonometric polynomials and reduced integration, Schneider [49] and Vondřej et al. [56], which behave very similar to trilinear finite elements with reduced integration, see Schneider et al. [50]. To each element which is completely contained in a single material phase we associate the corresponding hyperelastic stored energy function to the Gauss point. Elements containing interfaces are furnished with so-called composite voxel properties, see Ospald et al. [28], i.e. the effective hyperelastic properties of a laminate consisting of the materials contained in the element, and the direction of lamination corresponding to the (linearized) material interface. Using composite voxels significantly increases the accuracy of Cartesian grid-based computational homogenization results, see Kabel et al. [27] and Ospald et al. [28]. In particular, a

much lower number of elements suffices to reach the desired accuracy.

The original idea of Moulinec-Suquet [41] consists of rewriting the equilibrium equation (2.2) as a perturbation of a non-physical problem with a constant coefficient  $c_0 > 0$ ,

$$\text{Div} [P(F)] = 0 \Leftrightarrow c_0 \text{Div} \nabla u = -\text{Div} [P(F) - c_0 F]$$

with  $F = \bar{F} + \nabla u$ . As  $u$  is periodic, the left hand side can be inverted in terms of Fourier series. Writing  $G^0 = (c_0 \text{Div} \nabla)^{-1}$ , we arrive at the equation

$$u = -G^0 \text{Div} [P(F) - c_0 F],$$

which can be equivalently rewritten in terms of the local deformation gradient  $F$

$$F + \Gamma^0 [P(F) - c_0 F], \quad \Gamma^0 = \nabla G^0 \text{Div}. \tag{4.1}$$

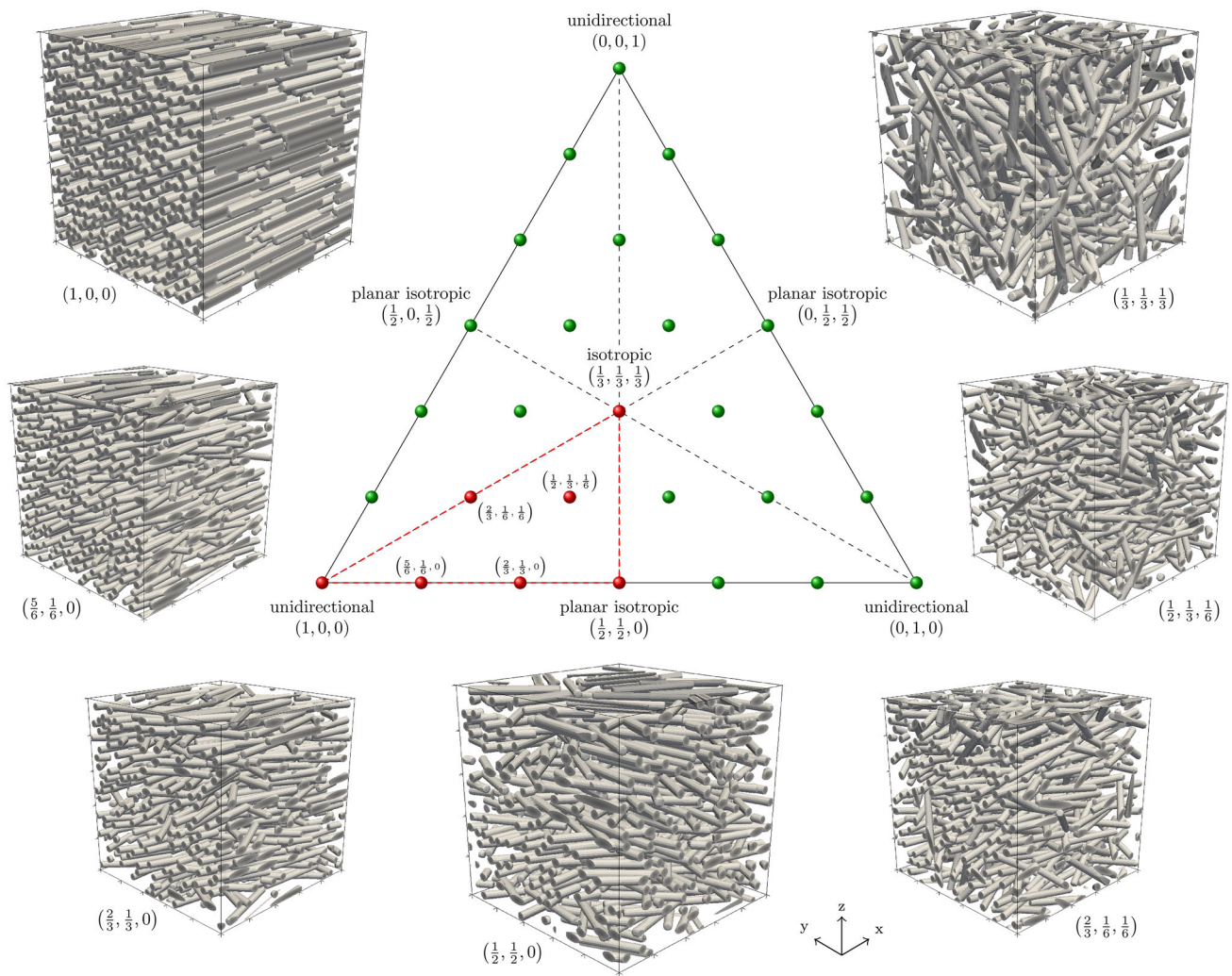


**Fig. 2** Visualization of the diagonal components of a second order fiber orientation tensor in the unit simplex. Computer generated RVEs using the ACG distribution are shown for some moments within the red

sub-triangle, marked by *red bullets*. All other fiber orientation states can be obtained by orthogonal transformations. (Color figure online)

The latter equation is known as the Lippmann-Schwinger equation in hyperelasticity and, for proper choice of  $c_0$ , gives rise to a fixed point method to solve the equilibrium equation (2.2) [25,30]. The operator  $\Gamma^0$  has an explicit expression in terms of Fourier coefficients [30], giving rise to a solution method which requires only storing the deformation gradient  $F$  in memory. In particular, an assembling of the system matrix is not necessary.

As a consequence, comparatively large computations can be carried out with modest memory requirements. There is also a variant of this Lippmann-Schwinger equation accounting for mixed boundary conditions, see Kabel et al. [26] for the technical details.

### 4.3 Setting up a model transversely isotropic energy

For the fiber (f) and the matrix (m) phases we choose neo-Hookean energy densities

$$W_m = \frac{G_m}{2} (J_1 - 3) + \frac{K_m}{2} (J_3 - 1)^2 \quad \text{and}$$

$$W_f = \frac{G_f}{2} (J_1 - 3) + \frac{K_f}{2} (J_3 - 1)^2,$$

with  $J_1 = J_3^{-2/3} \text{tr}(F^T F)$  and  $J_3 = \det F$ . The shear and bulk moduli selected, see Table 2, correspond to those of polypropylene and e-glass, taken from the experimental data of Fliegner et al. [13].

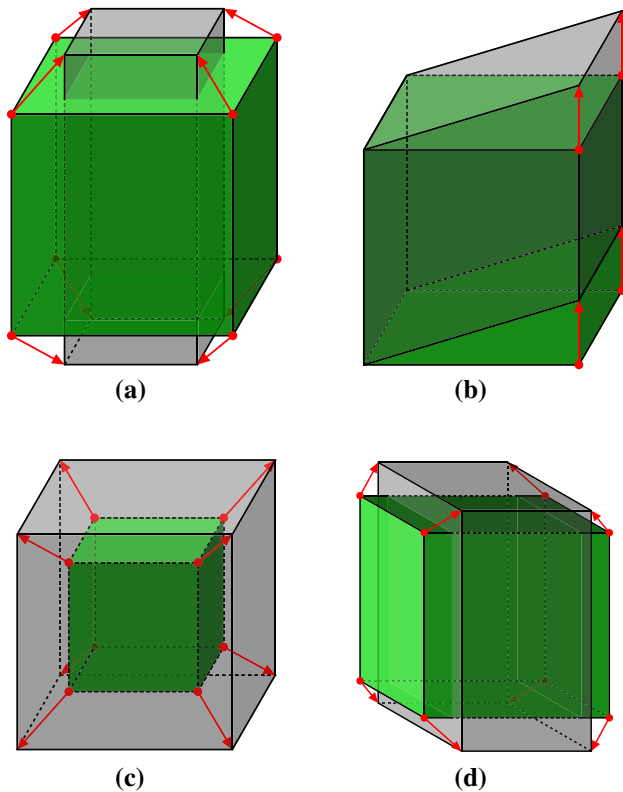


**Fig. 3** Deformation modes considered for the training data. **a** Uniaxial ext. ( $D_1$ ). **b** Shear ( $D_2$ ). **c** Volumetric ext. ( $D_3$ ). **d** Planar ext. ( $D_4$ )

**Table 1** Boundary conditions for the different deformations of Fig. 3a–d

Uniaxial extension ( $D_1$ ):	
$\begin{bmatrix} P_{11} = 0 & F_{12} = 0 & F_{13} = 0 \\ F_{21} = 0 & P_{22} = 0 & F_{23} = 0 \\ F_{31} = 0 & F_{32} = 0 & F_{33} = \lambda \end{bmatrix}$	$\lambda \in [1, 1.3]$
Shear ( $D_2$ ):	
$\begin{bmatrix} F_{11} = 1 & F_{12} = 0 & F_{13} = 0 \\ F_{21} = 0 & F_{22} = 1 & F_{23} = \kappa \\ F_{31} = 0 & F_{32} = 0 & F_{33} = 1 \end{bmatrix}$	$\kappa \in [0, 0.3]$
Volumetric extension ( $D_3$ ):	
$\begin{bmatrix} F_{11} = \lambda & F_{12} = 0 & F_{13} = 0 \\ F_{21} = 0 & F_{22} = \lambda & F_{23} = 0 \\ F_{31} = 0 & F_{32} = 0 & F_{33} = \lambda \end{bmatrix}$	$\lambda \in [1, 1.2]$
Planar extension ( $D_4$ ):	
$\begin{bmatrix} P_{11} = 0 & F_{12} = 0 & F_{13} = 0 \\ F_{21} = 0 & F_{22} = \lambda & F_{23} = 0 \\ F_{31} = 0 & F_{32} = 0 & F_{33} = \lambda \end{bmatrix}$	$\lambda \in [1, 1.3]$

As the starting point of the orientation averaging procedure we use the transversely isotropic material model of Goldberg et al. [18]

$$W(F, p) = \frac{\alpha_1}{2}(J_1 - 3) + \frac{\alpha_2}{2}(J_3 - 1)^2 + \alpha_3 \left( I_4(p) + 2I_4(p)^{-\frac{1}{2}} - 3 \right), \quad (4.2)$$

**Table 2** Material parameters for the matrix ( $m$ ) and fiber ( $f$ ) material

$G_m$ [GPa]	$K_m$ [GPa]	$G_f$ [GPa]	$K_f$ [GPa]
0.56	2.35	29.66	36.46

with the invariant  $I_4(p) = C : p \otimes p \equiv \|Fp\|^2$ , which depends on three positive material parameters  $\alpha = (\alpha_1, \alpha_2, \alpha_3)$ . The first two terms of (4.2) correspond to the shear and bulk moduli of a neo-Hookean material and are supposed to cover the isotropic behavior of the composite, whereas the third term takes into account the fibers' influence, resembling uniaxial incompressible extension of a neo-Hookean material. The second Piola-Kirchhoff stress  $S_p$  computes as

$$S_p = \alpha_1 J_3^{-\frac{2}{3}} \text{dev}(C)C^{-1} + \alpha_2 J_3(J_3 - 1)C^{-1} + 2\alpha_3 \left( 1 - I_4(p)^{-\frac{3}{2}} \right) p \otimes p,$$

cf. Goldberg et al. [18]. To take into account the fiber orientation distribution we apply orientation averaging with the ACG distribution (3.6), resulting in

$$S_B = \alpha_1 J_3^{-\frac{2}{3}} \text{dev}(C)C^{-1} + \alpha_2 J_3(J_3 - 1)C^{-1} + 2\alpha_3 \sum_{i=1}^N w_i \left( 1 - (t_i^T C t_i)^{-\frac{3}{2}} \right) t_i \otimes t_i, \quad (4.3)$$

and the Cauchy stress tensor arises from the push-forward

$$\sigma_B = J_3^{-1} F S_B F^T.$$

### 4.4 Fitting strategy

Suppose there is a set of fiber orientations  $A_1, \dots, A_{n_F}$  with corresponding  $B$ -tensors  $B_a, \dots, B_{n_F}$  which is sufficiently dense in the fiber orientation triangle, cf. Fig. 2. Suppose that for each such orientation, a number  $n_L$  of load cases was computed numerically, leading to pairs of deformation gradients and Cauchy stresses  $(\bar{F}_{ij}, \bar{\sigma}_{ij})$  for fiber orientation indices  $i = 1, \dots, i_{n_F}$  and loading indices  $j = 1, \dots, n_L$ .

We wish to determine the parameters  $\alpha$  of the model (4.2), s.t. the computed Cauchy stress  $\sigma_{B_i}(\bar{F}_{ij})$  is as close as possible to the computed Cauchy stress  $\bar{\sigma}_{ij}$ . For that purpose, we minimize the variation of the relative stress error

$$\frac{1}{n_F n_L} \sum_{i=1}^{n_F} \sum_{j=1}^{n_L} \frac{\|\sigma_{B_i}(\bar{F}_{ij}) - \bar{\sigma}_{ij}\|^2}{\|\bar{\sigma}_{ij}\|^2} \quad (4.4)$$

where we use the Frobenian norm  $\|S\|^2 \equiv \text{tr}(S^T S)$  for the stress. We utilize this form because it is quadratic in the stresses  $\sigma_{B_i}(\bar{F}_{ij})$ . In particular, if the parameters to be fitted enter the energy only as linear factors of some predefined



**Table 3** Relative errors  $\mathcal{D}$  for fittings with different energy densities

Energy density	Ansatz	$\alpha_1$ [GPa]	$\alpha_2$ [GPa]	$\alpha_3$ [GPa]	$\mathcal{D}$ [%]	$\frac{\mathcal{D}-\mathcal{D}_{ref}}{\mathcal{D}_{ref}}$ [%]
$W_{ref}$	$\alpha_3(I_4 + 2I_4^{-\frac{1}{2}} - 3)$	0.934	2.985	0.958	4.414	0.0
$W_1$	$\alpha_3(I_4^{-1} + 2I_4^{\frac{1}{2}} - 3)$	0.919	3.064	1.077	5.390	22.111
$W_2$	$\alpha_3(I_4 - 1)^2$	0.996	2.919	0.456	7.759	75.781
$W_3$	$\alpha_3(\bar{I}_4 + 2\bar{I}_4^{-\frac{1}{2}} - 3)$	1.153	2.986	0.920	11.684	164.700
$W_4$	$\alpha_3(K_1 - 1)$	1.356	3.467	0.102	23.636	435.470

energies, like in the Goldberg form (4.2), the optimality system for minimizing (4.4) is linear and thus readily inverted.

In the numerical demonstration Sect. 5; Table 3, we will compare the performance of energy (4.2) to different proposals in the literature.

### 5 Numerical demonstration

#### 5.1 Documentation of the set-up

We have discretized the fiber orientation triangle uniformly, cf. Fig. 4a, leading to a total of  $n_F = 91$  fiber orientations. For each of these fiber orientations, a volume element was generated using the random sequential adsorption algorithm [12,57] for spherocylinders with an aspect ratio of 10 and a fiber volume fraction of 20%. The volume elements were assumed cubical with an edge length of twice the fibers' length, each one incorporating 210 fibers. Examples of such generated structures are depicted in Fig. 2. In Goldberg et al. [18] it was shown that a volume element with twice the fibers' length is representative for tension in fiber direction of a unidirectional hyperelastic composite. As precisely this loading case represents the situation with the highest contrasts and the most severe deformation, twice the fibers' length constitutes a sufficient dimension for a representative volume element for the other orientation states.

Then, each of these 91 volume elements was discretized by a regular Cartesian grid with  $64^3$  elements. To take into account the exact position of the interfaces, the model order reduction method of Ospald et al. [28] was used, where each voxel containing a material interface gets assigned an appropriately rotated effective hyperelastic energy corresponding to a hyperelastic laminate. This method significantly reduces the number of elements required for obtaining an accurate effective elastic stress response, see Ospald et al. [28] for details.

Then, each of these discretized elements was subjected to the loading scenarios depicted in Fig. 3a–d in five equally distributed loading steps, and solved by the basic scheme for hyperelasticity (4.1) and the staggered grid discretization [51] until the convergence criterion

$$\|F^{n+1} - F^n\|/\|\bar{F}\| \leq .5 \times 10^{-4},$$

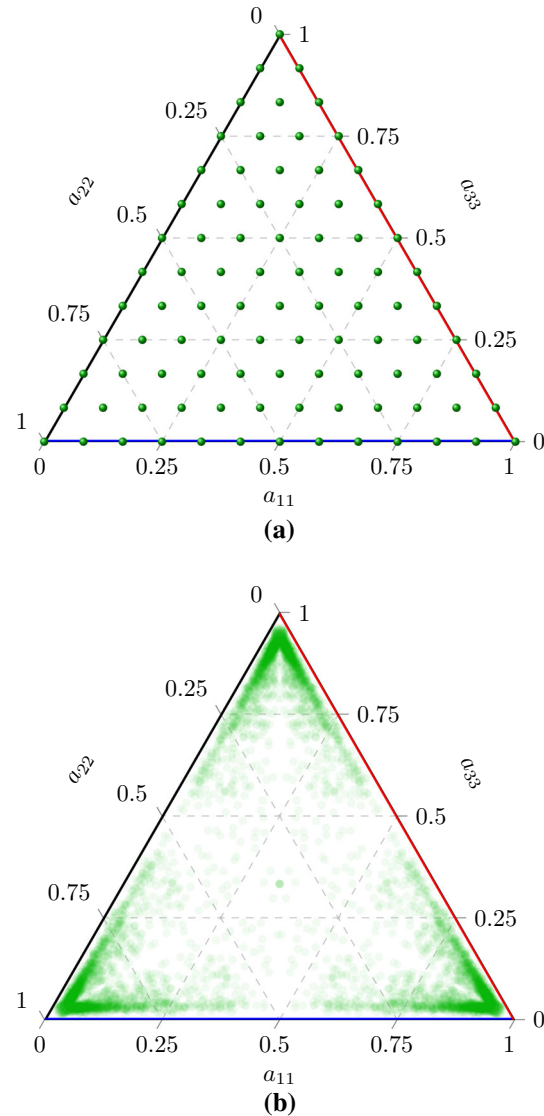


**Fig. 4** Fiber orientation states used for generation of volume elements and parameter identification as well as fiber orientations (eigenvalues of  $A$ ) present in the chain link depicted in Fig. 7a. **a** Fiber orientations used for parameter identification. **b** Fiber orientations present in the filled chain link part

was satisfied. For each of the 91 orientations and the four different load scenarios, the computation of the five load steps took between 23 and 860 s (78 s on average) on a workstation with 4 Intel Xeon E7-4880 v2 CPUs (15 cores each, 38400

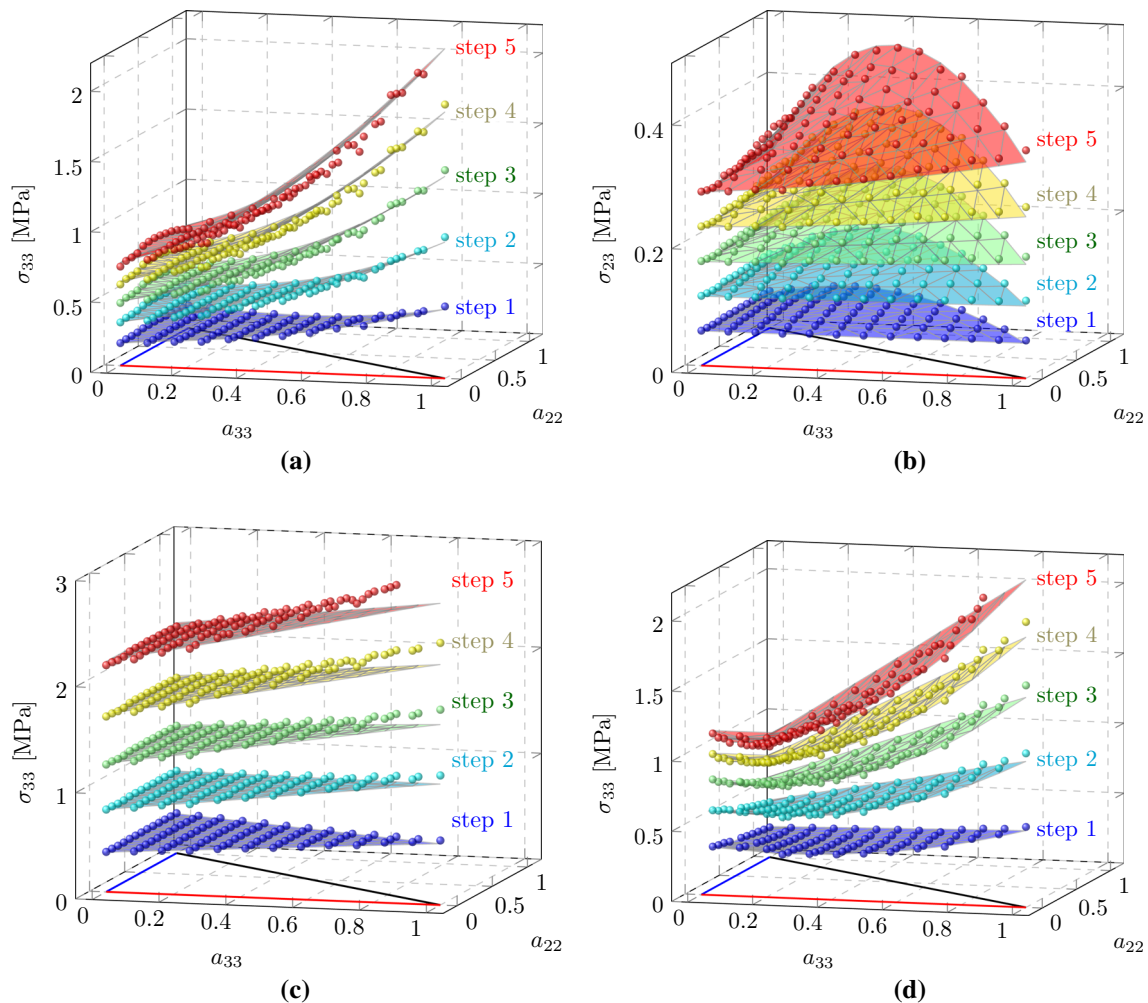


**Fig. 5** Comparison of identified material model (surface plot) with RVE data (bullets) for all four deformations. **a** Uniaxial extension in  $z$ -direction. **b** Shearing in the  $y$ - $z$ -plane. **c** Volumetric extension in the  $y$ - $z$ -plane. **d** Planar extension in the  $y$ - $z$ -plane

KB cache), and 32 threads OpenMP, using the OpenMP-parallel C++ implementation of FFT-based computational homogenization at TU Chemnitz, see Ospald et al. [28].

## 5.2 Identification of the model coefficients and comparison to other model strain energy density functions

The data whose generation was described in the previous section formed the basis for the fitting of the Tucker-averaged hyperelastic energy function (3.2) and (3.4), respectively.

The dominant scalar stress values are plotted in Fig. 5 as bullets, for each of the four deformations (different images) and each of the five load steps (different heights in one figure). For the identification we choose  $N = 210$  Gauss points on the sphere, see Fig. 1a, with corresponding quadrature weights  $w_i$  computed with the help of the corresponding Voronoi diagrams (cf. [15]). We will see in the next section that a lower number of Gauss points already provides sufficient

accuracy for the ansatz (4.2). However, we wish to assess the performance of other transversely isotropic stored energy functions occurring in the literature without worrying about integration accuracy.

For the comparison we keep the first two terms of (4.2), which correspond to an isotropic neo-Hookean energy density, and only vary the third term encoding the anisotropic effects. The densities  $W_2$  and  $W_4$  are proposed in Balzani's work [6]. They both allow an exact analytical averaging, noticing

$$\int_{S^2} (I_4 - 1)^2 \psi(p) dS(p) = C : \mathbb{A} : C - 2C : A + 1,$$

and

$$\begin{aligned} \int_{S^2} (K_1 - 1) \psi(p) dS(p) \\ = \int_{S^2} (I_5 - I_1 I_4 + I_2 - 1) \psi(p) dS(p) \end{aligned}$$

**Table 4** Identified material parameters and relative errors  $\mathcal{D}$  for different fittings

Row	Variations	$\alpha_1$ [GPa]	$\alpha_2$ [GPa]	$\alpha_3$ [GPa]	$\mathcal{D}$ [%]	$\frac{\mathcal{D}-\mathcal{D}_{\text{ref}}}{\mathcal{D}_{\text{ref}}}$ [%]
1	All orientations (91)	0.934	2.985	0.958	4.414	0.0
2	Only UD	0.992	3.009	1.019	6.325	43
3	UD and isotropic	0.971	2.992	1.016	5.580	26
4	UD + iso + iso planar	0.949	2.971	0.980	4.618	4.6
5	$D_1$	0.907	2.901	0.929	5.368	21
8	$D_1, D_2$	0.898	3.019	0.947	5.004	13
9	$D_1, D_3$	0.907	2.901	0.929	5.368	21
10	Up to 4th step	0.944	2.978	0.971	4.489	1.7
11	Up to 3rd step	0.946	2.984	0.970	4.501	2.0
12	Up to 2nd step	0.950	2.990	0.967	4.513	2.2
13	Up to 1st step	0.954	2.996	0.961	4.521	2.4

$$= C^2 : A - I_1(C : A) + I_2 - 1.$$

$W_3$  is similar to  $W_{\text{ref}}$  but instead of averaging the energy density, only the invariant  $I_4$  is averaged, leading to

$$\begin{aligned} \bar{I}_4 &= \int_{S^2} I_4 \psi(p) dS(p) \\ &= \int_{S^2} C : p \otimes p \psi(p) dS(p) = C : A, \end{aligned}$$

the Frobenian inner product of the right Cauchy–Green tensor  $C$  and the fiber orientation tensor  $A$  of second order. For this approach, advocated in Freed [14] and Gasser [16], no integration on the sphere is necessary. In particular, the evaluation of  $W_3$  is comparatively fast.  $W_1$ , like  $W_{\text{ref}}$ , is motivated by an uniaxial incompressible extension of a neo-Hookean material, but is designed to mimic the behavior of the second basic invariant  $I_2$ .

The results of minimizing the objective (4.4) are listed in Table 3, both in terms of the identified parameters and the associated root mean square (RMS)  $\mathcal{D}$ , defined by

$$\mathcal{D} = \sqrt{\frac{1}{n_F n_L} \sum_{i=1}^{n_F} \sum_{j=1}^{n_L} \frac{\|\sigma_{B_i}(\bar{F}_{ij}) - \bar{\sigma}_{ij}\|^2}{\|\bar{\sigma}_{ij}\|^2}}. \tag{5.1}$$

The lowest value of  $\mathcal{D}$ ,  $\approx 4.14\%$ , is reached for  $W_{\text{ref}}$ . Among the additional energies,  $W_1$  comes closest to  $W_{\text{ref}}$ , but the RMS already deviates by 22%. The second density  $W_2$  reaches almost twice the RMS of  $W_{\text{ref}}$ . As already explained, its simple polynomial character permits an exact analytical averaging. However, the associated second Piola–Kirchhoff stress is linear in  $I_4$ , and thus cannot reproduce the nonlinear behavior of the composite material.  $W_3$  leads to an almost tripled RMS compared to  $W_{\text{ref}}$ . Using the averaging approach of Freed [14] and Gasser [16] appears not applicable to composites. Finally,  $W_4$  performs worst in this comparison, with more than four times the RMS of  $W_{\text{ref}}$ .

To summarize, Tucker-averaging the energy density  $W_{\text{ref}}$  leads to the lowest average stress error among the considered energy densities, which is, on average, well below 5%. In Fig. 5 we plot the dominant coefficients of the Cauchy stress tensor for each deformation and compare the identified material model (Table 4 row 1) to the data obtained by FFT-based computational homogenization. All four subplots exhibit good accordance of material model and computational data. The material model is capable of reproducing both the qualitative and the quantitative stress distribution over the fiber orientations.

### 5.3 Reducing the number of Gauss points

In the previous section we explicitly neglected the influence of the number of Gauss points. As we have the application of the derived material model to computing the hyperelastic component in mind, the integration of the derived material model in a user-defined material routine and the associated computational cost play an important role for our investigation. Therefore, we have generated different sets of Gauss point with associated Gauss weights, ranging from two Gauss points up to 632 Gauss points, and minimized the objective  $\mathcal{D}$  using the energy  $W_{\text{ref}}$ , see (5.1), for each of these sets. The associated minimal values are plotted in Fig. 6. It can be seen that with increasing number of Gauss points, the minimal RMSs decrease monotonously, up to a plateau at about  $\mathcal{D} \approx 4.414\%$ . Thus, we see that  $N = 32$  Gauss points already suffice for reaching the minimal RMS. Furthermore, increasing the number of Gauss points further does not lead to a noticeable decrease in the average relative error.

This small number of Gauss points,  $N = 32$ , is remarkable in itself, and results from the transformation of the Gauss points according to (3.5). If non-orientation-adapted Gaussian integration is used, about 10 times the number of Gauss points are required to reach a lower accuracy, compare Li et al. [32].

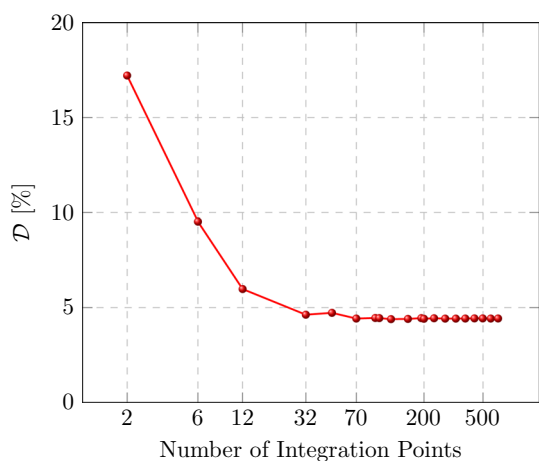


**Fig. 6** Difference of material model and RVE data for different sets of integration points

#### 5.4 Sensitivity analysis

In this paragraph we study whether all fiber orientations, the four loading scenarios, cf. Figure 3a–d, and the five load steps are really necessary for the identification. Indeed, if some of those could be left out, we could accelerate the computations.

The data is collected in Table 4, and the first row shows the result for a complete fitting, meaning when we employ all 1820 stress tensors and yields the relative error  $\mathcal{D}_{\text{ref}} = 4.414\%$ .

First, we study the influence of the fiber orientation. If only the unidirectional (UD) fiber orientation state is used for the minimization, the average relative stress  $\mathcal{D}$  is about 50% higher than if all fiber orientations are taken into account. Notice that this scenario corresponds to the usual grain-based homogenization process [29], where only a material model is fitted to the unidirectional fiber orientation, and the other fiber orientation states are covered by subsequent averaging of the UD response. Already at small strains, it is known that such a procedure is error-prone, see Müller et al. [44]. Leaving the parameters for the UD model “free” and identifying them for all fiber orientations at the same time leads to much better results.

Taking into account both the UD and the isotropic fiber orientation states decreases the average relative error  $\mathcal{D}$  significantly, and further incorporating the planar isotropic fiber orientation state leads to a RMS which is already very close to the result computed with all 91 different fiber orientation states.

In a second study, we use all fiber orientations but only subsets of the four deformations. Here a combination of uniaxial extension  $D_1$  and shear loading  $D_2$  comes closest to  $\mathcal{D}_{\text{ref}}$ , but still holds a relative difference of around 13%. Notice that it is neither possible to solely rely on shear loading  $D_2$  or volumetric extension  $D_3$  for the identification of all three material

parameters  $\alpha_1$ ,  $\alpha_2$  and  $\alpha_3$ , because for these loadings some summands in (4.2) contribute nothing to the energy density.

Last but not least we vary the number of load steps, i.e. we identify only for smaller deformations as we leave out the last load steps. Here we see that even a fitting to only 20% of the given amplitude yields a relative difference smaller than 3%.

To sum up, for the identification of the material model, only the “extreme” fiber orientation states uni-directional, planar isotropic and isotropic are dominating. Furthermore, as the composite behaves approximately neo-Hookean when loaded in a fixed direction, not all five load steps are strictly necessary.

As can be seen from Table 5 using only these three “extreme” fiber orientation states also gives an computational speedup of factor 36 compared to using all 91 fiber orientations.

#### 5.5 Application to an injection-molded chain link

In this final paragraph we used the material model with fitted coefficients from Table 4 to conduct a finite element analysis of a chain link used for conveyor belts, see Fig. 7 for the CAD geometry. For the production, it is possible to choose four different injection points. To study an extreme case, we chose only one injection point.

To obtain the fiber orientation within the chain link, we rely upon an injection molding simulation carried out using the *OpenFOAM*-based *injectionMoldingFoam* solver, see Ospald [46] for details. The distribution of the resulting fiber orientations’ eigenvalues within the fiber orientation triangle is shown in Fig. 4b. For each element, a graffiti was sprayed into the fiber orientation triangle. Thus, the relative frequency of occurrence is proportional to the shading in the figure.

We chose the isotropic fiber orientation tensor as initial condition at the inlet, which is why it appears in Fig. 4b. Then, during the flow, the fiber orientation quickly approaches an almost planar state. Indeed, almost all fiber orientations are concentrated close to the line connecting an almost unidirectional and an almost planar isotropic state.

For the finite element analysis we use the commercial software *ABAQUS* 6.14–1. The material model is integrated into an *ABAQUS* user-defined material function (*UMAT*), relying on solution dependent variables (*SDV*), which are introduced by the user routine *SDVINI*. Given the fiber orientation tensor  $A$ , the latter user routine reads the untransformed fiber directions  $\{p_i\}$  and the corresponding weights  $w_i$  from a text file, determines the transformed directions  $\{t_i\}$  and stores them as *SDV*. The effective stress, together with the material tangent, is computed using (3.5) and (4.3).

For the analysis, we apply an external force  $F = 100$  N to the inner sides of the shafts, compare Fig. 7a. The geometry is discretized by 102257 10-node, i.e. quadratic, tetrahedra,

**Table 5** Runtime of the RVE simulations for obtaining  $\bar{\sigma}_{ij}$  for different sets of fiber orientations and all experiments  $D_1, \dots, D_4$

Row	Variations	# Of simulations	Runtime [min]	Speedup
1	All orientations (91)	364	474	1
2	Only UD	4	4.7	101
3	UD and isotropic	8	9.6	49
4	UD + iso + iso planar	12	13.3	36

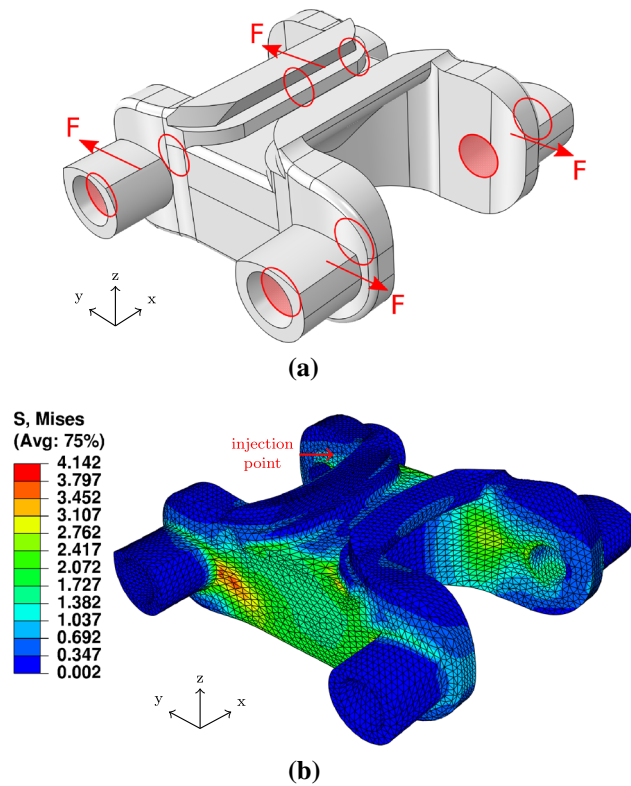


**Fig. 7** External forces applied to the chain link as well as mesh and stress field. **a** External forces applied to the chain link. **b** Mesh and von Mises stress field

associated to the element type *C3D10* in *ABAQUS*, resulting in 409028 integration points.

The computations were run on a desktop computer with a *Intel i7-3770 CPU @3.40 GHz* (4 cores) and 16 GB RAM @1333 MHz, and took 770s with  $N = 210$  fiber directions  $\{t_i\}$ . Figure 7b shows the resulting von Mises stress field in the deformed chain link. The comparison of deformed and undeformed geometry reveals a large deformation pointing out the necessity of a hyperelastic material. It can be seen that the stress accumulates at the flanks of the chain link as the fibers are aligned in parallel to the direction of the external forces in those areas. The fibers in the chain link’s middle part, however, are smaller because they are mostly aligned orthogonally to the external forces. Figure 9 illustrates both the fiber orientation and the von Mises stress field in the chain link’s middle plane. Here, too, the stresses reach their

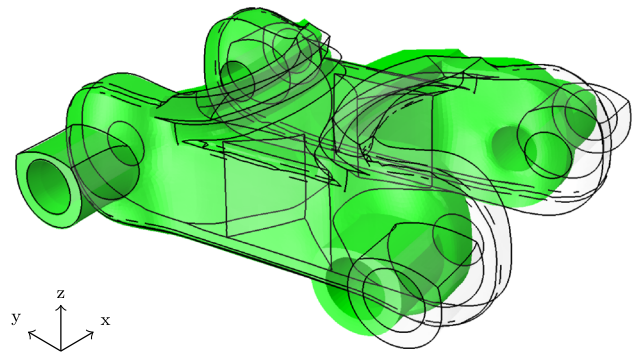


**Fig. 8** Comparison of chain link’s deformation with (green) and without (white) anisotropic term in material model. (Color figure online)

maximum in areas where the majority of the fibers is aligned in the direction of the external forces. The principal fiber orientation degree *OD* in Fig. 9a is defined as

$$OD = \frac{3}{2} \lambda_{\max} - \frac{1}{2} \in [0, 1]$$

where  $\lambda_{\max}$  denotes the largest eigenvalue of  $A$ , which is always greater equal than  $\frac{1}{3}$ . Consequently  $OD = 0$  corresponds to an isotropic and  $OD = 1$  to a unidirectional fiber orientation. The principal fiber orientation in Fig. 9b is the eigenvector associated to  $\lambda_{\max}$  scaled by *OD*.

Last but not least we compare our fully anisotropic model to the response computed by an isotropic neo-Hookean model which we fit to our training data. Comparing both deformed structures, see Fig. 8, exhibits drastic differences. The chain link has a length of  $l_0 = 37.4$  mm in the undeformed configuration. The length in the deformed configurations becomes  $l_{iso} = 52.2$  mm and  $l_{aniso} = 47.9$  mm respectively. We conclude that taking into account the material’s anisotropy is crucial for predicting the deformation.

## 6 Summary and outlook

This article was devoted to studying a fiber orientation-adapted integration scheme for Tucker’s orientation averaging procedure applicable to non-linear material laws, which is stable w.r.t. fiber orientations degenerating into planar states.

We have established a reference scenario for fitting the Tucker average of a transversely isotropic hyperelastic

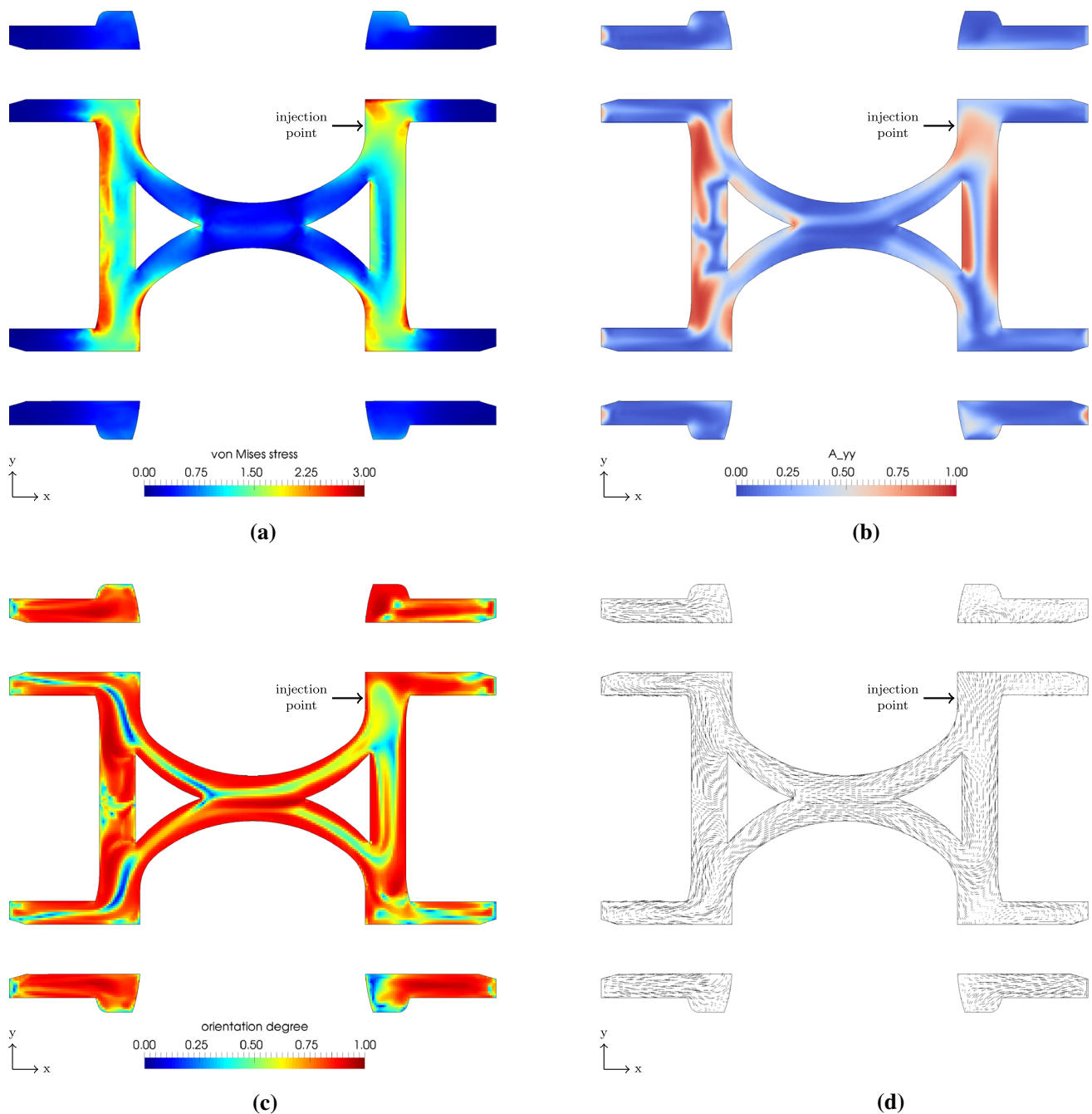


**Fig. 9** Visualization of fiber orientation and von Mises stress in a cross section of the part. **a** von Mises stress. **b** Second order fiber orientation tensor component  $A_{yy}$ . **c** Principal fiber orientation degree. **d** Principal fiber orientation

energy, corresponding to a uni-directional fiber orientation, to microstructural simulations, obtained by FFT-based computational homogenization.

The resulting hyperelastic material map turns out to be surprisingly accurate, simple to integrate in commercial finite element codes and fast in its execution.

From a theoretical point of view it would be interesting to investigate further which transversely isotropic hyperelastic stored energy functions possess good structural properties

(like quasi-convexity), while at the same time providing effective properties that can be fitted accurately to experimental or computational data.

A purely elastic description of the mechanical behavior of fiber reinforced composites does not accurately model the various phenomena involved. Thus, the elastic considerations of this article should be considered a starting point for more investigations involving more elaborate material behavior. For instance, it would be interesting to see whether

the proposed method can be used to accurately predict the effective behavior of composites with constituents undergoing viscoelastic or elastoplastic behavior at finite strains.

**Acknowledgements** Niels Goldberg and Felix Ospald acknowledge support from the German Research Foundation (DFG) via the Federal Cluster of Excellence EXC 1075 “MERGE Technologies for Multifunctional Lightweight Structures”. We thank the professorship in Materials-Handling Technology (Fördertechnik) at TU Chemnitz for sharing the CAD geometry of the chain link.

## Appendix

### A Derivation of the integral transformation formula

This section is devoted to derive the identity (3.5), i.e.

$$\int_{S^2} \psi_B(p) W(p) dS(p) = \frac{1}{4\pi} \int_{S^2} W(t(p)) dS(p) \quad (A.1)$$

where  $W$  is a function on the sphere  $S^2$ ,  $t(p) = \frac{B^{-\frac{1}{2}}p}{\|B^{-\frac{1}{2}}p\|}$ ,  $\psi_B = \frac{1}{4\pi} (p^T B p)^{-\frac{3}{2}}$ , and  $B$  is a symmetric positive definite  $3 \times 3$  matrix with determinant 1. Before coming to the gist of argument, notice the identity

$$\int_0^\infty r^2 e^{-\frac{a}{2}r^2} dr = \frac{1}{a^{\frac{3}{2}}} \frac{\sqrt{2\pi}}{2}, \quad (A.2)$$

which is an immediate consequence of integrating the identity

$$\frac{d}{dr} \left( r e^{-\frac{a}{2}r^2} \right) = e^{-\frac{a}{2}r^2} - ar^2 e^{-\frac{a}{2}r^2}.$$

The derivation of (A.1) is based upon the successive rewriting

$$\begin{aligned} & \frac{1}{4\pi} \int_{S^2} W(p) (p^T B^{-1} p)^{-\frac{3}{2}} dS(p) \\ &= \frac{1}{(2\pi)^{\frac{3}{2}}} \int_{S^2} W(p) \frac{1}{(p^T B^{-1} p)^{\frac{3}{2}}} \frac{\sqrt{2\pi}}{2} dS(p) \\ &= \frac{1}{(2\pi)^{\frac{3}{2}}} \int_{S^2} W(p) \int_0^\infty r^2 e^{-\frac{r^2}{2} p^T B^{-1} p} dr dS(p) \\ &= \frac{1}{(2\pi)^{\frac{3}{2}}} \int_{\mathbb{R}^3} W\left(\frac{x}{\|x\|}\right) e^{-\frac{1}{2}x^T B^{-1}x} dx, \end{aligned}$$

where we made use of (A.2) with  $a = p^T B^{-1} p$ . Thus, the left hand side of (A.1) can be expressed by a free space integral involving a Gaussian. Changing variables  $x = B^{-\frac{1}{2}}y$  in this integral yields

$$\begin{aligned} & \frac{1}{(2\pi)^{\frac{3}{2}}} \int_{\mathbb{R}^3} W\left(\frac{B^{-\frac{1}{2}}y}{\|B^{-\frac{1}{2}}y\|}\right) e^{-\frac{1}{2}\|y\|^2} dy \\ &= \frac{1}{(2\pi)^{\frac{3}{2}}} \int_{S^2} W\left(\frac{B^{-\frac{1}{2}}p}{\|B^{-\frac{1}{2}}p\|}\right) \\ & \int_0^\infty r^2 e^{-\frac{r^2}{2} \frac{p^T B^{-1} p}{\|B^{-1/2}p\|^2}} dr dS(p) \\ &= \frac{1}{(2\pi)^{\frac{3}{2}}} \int_{S^2} W(t(p)) \frac{\sqrt{2\pi}}{2} \left[ \frac{p^T B^{-1} p}{\|B^{-\frac{1}{2}}p\|^2} \right]^{-\frac{3}{2}} dS(p) \\ &= \frac{1}{4\pi} \int_{S^2} W(t(p)) dS(p), \end{aligned}$$

which shows the identity (A.1).

## References

- Autodesk, Inc., Moldflow. <http://www.autodesk.com/moldflow>. Accessed: 2016-09-07
- CoreTech System Co., Ltd., Moldex3D. <http://www.moldex3d.com>. Accessed: 2016-09-07
- SIGMA Engineering GmbH, SIGMASOFT. <http://www.sigmasoft.de>. Accessed: 2016-09-07
- Aboudi J (2004) The generalized method of cells and high-fidelity generalized method of cells micromechanical models – a review. *Mech Adv Mater Struct* 11(4–5):329–366
- Advani SG, Tucker CL (1987) The use of tensors to describe and predict fiber orientation in short fiber composites. *J Rheol* 31(8):751–784. doi:10.1122/1.549945
- Balzani D, Neff P, Schröder J, Holzapfel G (2006) A polyconvex framework for soft biological tissues. Adjustment to experimental data. *Int J Solids Struct* 43(20):6052–6070
- Bažant P, Oh BH (1986) Efficient numerical integration on the surface of a sphere. *ZAMM - J Appl Math Mech / Zeitschrift für Angew Math und Mech* 66(1):37–49
- Benveniste Y (1987) A new approach to the application of Mori-Tanaka’s theory in composite materials. *Mech Mater* 6:147–157
- Dinh SM, Armstrong RC (1984) A rheological equation of state for semiconcentrated fiber suspensions. *J Rheol* 28(3):207–227. doi:10.1122/1.549748
- Eshelby J (1957) The determination of the elastic field of an ellipsoidal inclusion, and related problems. *Proc R Soc A* 241(1226):376–396
- Eshelby J (1959) The elastic field outside an ellipsoidal inclusion. *Proc R Soc A* 252(1271):561–569
- Feder J (1980) Random sequential adsorption. *J Theor Biol* 87(2):237–254
- Fliegerer S, Luke M, Gumbsch P (2014) 3D microstructure modeling of long fiber reinforced thermoplastics. *Compos Sci Technol* 104:136–145
- Freed AD, Einstein DR, Vesely I (2005) Invariant formulation for dispersed transverse isotropy in aortic heart valves: an efficient means for modeling fiber splay. *Biomech Modeling Mechanobiol* 4(2–3):100–117
- Freund M (2013) Verallgemeinerung eindimensionaler Materialmodelle für die Finite-Elemente-Methode, Technische Universität Chemnitz / Berichte aus der Professur Festkörpermechanik, vol. 336. VDI-Verl., Düsseldorf

16. Gasser TC, Ogden RW, Holzapfel GA (2006) Hyperelastic modelling of arterial layers with distributed collagen fibre orientations. *J R Soc Interface* 3(6):15–35
17. Geymonat G, Müller S, Triantafyllidis N (1993) Homogenization of nonlinearly elastic materials, microscopic bifurcation and macroscopic loss of rank-one convexity. *Arch Ration Mech Anal* 122(3):231–290. doi:[10.1007/BF00380256](https://doi.org/10.1007/BF00380256)
18. N. Goldberg, H. Donner, J. Ihlemann. (2015). Evaluation of hyperelastic models for unidirectional short fibre reinforced materials using a representative volume element with refined boundary conditions. *Technische Mechanik*. 35(2):80–99. [http://www.uni-magdeburg.de/ifme/zeitschrift\\_tm/2015\\_Heft2/02\\_Goldberg.html](http://www.uni-magdeburg.de/ifme/zeitschrift_tm/2015_Heft2/02_Goldberg.html)
19. Gräf M (2013) Efficient algorithms for the computation of optimal quadrature points on riemannian manifolds. *Universitätsverlag Chemnitz, Chemnitz*
20. Guedes JM, Kikuchi N (1990) Preprocessing and postprocessing for materials based on the homogenization method with adaptive finite element methods. *Comput Methods Appl Mech Eng* 83(2):143–198
21. Herzog R, Ospald F (2016) Optimal experimental design for linear elastic model parameter identification of injection molded short fiber-reinforced plastics. *Int J Numer Methods Eng*
22. Hill R (1965) A self-consistent mechanics of composite materials. *J Mech Phys Sol* 13:213–222
23. Hill R (1972) On constitutive macro-variables for heterogeneous solids at finite strain. *Proc R Soc London A: Math, Phys Eng Sci* 326(1565):131–147. doi:[10.1098/rspa.1972.0001](https://doi.org/10.1098/rspa.1972.0001)
24. Jeffery GB (1922) The motion of ellipsoidal particles immersed in a viscous fluid. *Proc R Soc London. Ser A* 102(715):161–179. doi:[10.1098/rspa.1922.0078](https://doi.org/10.1098/rspa.1922.0078)
25. Kabel M, Böhlke T, Schneider M (2014) Efficient fixed point and newton-krylov solvers for fft-based homogenization of elasticity at large deformations. *Comput Mech* 54(6):1497–1514. doi:[10.1007/s00466-014-1071-8](https://doi.org/10.1007/s00466-014-1071-8)
26. Kabel M, Fliegner S, Schneider M (2015) Mixed boundary conditions for fft-based homogenization at finite strains. *Comput Mech*
27. Kabel M, Merkert D, Schneider M (2014) FFT-based homogenization using composite voxels. *Comput Methods Appl Mech Eng*
28. Kabel M, Ospald F, Schneider M (2016) A model order reduction method for computational homogenization at finite strains on regular grids using hyperelastic laminates to approximate interfaces. *Comp Methods Appl Mech Eng* 309:476–496. doi:[10.1016/j.cma.2016.06.021](https://doi.org/10.1016/j.cma.2016.06.021)
29. Kammoun S, Doghri I, Adam L, Robert G, Delannay L (2011) First pseudo-grain failure model for inelastic composites with misaligned short fibers. *Compos Part A: Appl Sci Manuf* 42:1892–1902
30. Lahellec N, Michel JC, Moulinec H, Suquet P (2003) Analysis of inhomogeneous materials at large strains using fast fourier transforms. In: Miehe C (ed) IUTAM symposium on computational mechanics of solid materials at large strains, solid mechanics and its applications, vol 108. Springer, Netherlands, pp 247–258. doi:[10.1007/978-94-017-0297-3\\_22](https://doi.org/10.1007/978-94-017-0297-3_22)
31. Lebedev VI (1976) Quadratures on a sphere. *USSR Comput Math Math Phys* 16(2):10–24
32. Li Y, Stier B, Bednarczyk B, Simon JW, Reese S (2016) The effect of fiber misalignment on the homogenized properties of unidirectional fiber reinforced composites. *Mech Mater* 92:261–274
33. Lipscomb GI, Denn M, Hur D, Boger D (1988) Flow of fiber suspensions in complex geometries. *J Non-Newtonian Fluid Mech* 26(3):297–325. doi:[10.1016/0377-0257\(88\)80023-5](https://doi.org/10.1016/0377-0257(88)80023-5)
34. Michel JC, Suquet P (2003) Nonuniform transformation field analysis. *Int J Solids Struct* 40:6937–6955
35. Michel JC, Suquet P (2004) Computational analysis of nonlinear composite structures using the nonuniform transformation field analysis. *Comput Methods Appl Mech Eng* 193:5477–5502
36. Miehe C, Göktepe S, Lulei F (2004) A micro-macro approach to rubber-like materials - Part I: The non-affine micro-sphere model of rubber elasticity. *J Mech Phys Solids* 52:2617–2660
37. Miehe C, Koch A (2002) Computational micro-to-macro transitions of discretized microstructures undergoing small strains. *Arch Appl Mech* 72(4):300–317
38. Montgomery-Smith S, Jack D, Smith DE (2011) The fast exact closure for jeffery’s equation with diffusion. *J Non-Newtonian Fluid Mech* 166(7–8):343–353. doi:[10.1016/j.jnnfm.2010.12.010](https://doi.org/10.1016/j.jnnfm.2010.12.010)
39. Mori T, Tanaka K (1973) Average Stress in the Matrix and Average Elastic Energy of Materials with Misfitting Inclusions. *Acta Metall* 21:571–574
40. Mosby M, Matouš K (2016) Computational homogenization at extreme scales. *Extreme Mech Lett* 6:68–74
41. Moulinec H, Suquet P (1994) A fast numerical method for computing the linear and nonlinear mechanical properties of composites. *Comptes rendus de l’Académie des sciences. Série II, Mécanique, physique, chimie, astronomie* 318(11):1417–1423
42. Moulinec H, Suquet P (1998) A numerical method for computing the overall response of nonlinear composites with complex microstructure. *Comput Methods Appl Mech Eng* 157:69–94
43. Müller S (1987) Homogenization of nonconvex integral functionals and cellular elastic materials. *Arch R Mech Anal* 99(3):189–212. doi:[10.1007/BF00284506](https://doi.org/10.1007/BF00284506)
44. Müller V, Brylka B, Dillenberger F, Glöckner R, Kolling S, Böhlke T (2015) Homogenization of elastic properties of short-fiber reinforced composites based on measured microstructure data. *J Compos Mater*. doi:[10.1177/0021998315574314](https://doi.org/10.1177/0021998315574314)
45. Neukamm S, Schäffner M (2016) Quantitative homogenization in nonlinear elasticity for small loads. Preprint. [arXiv:1703.07947](https://arxiv.org/abs/1703.07947)
46. Ospald F (2014) Numerical simulation of injection molding using OpenFOAM. *Proc Appl Math Mech* 14(1):673–674. doi:[10.1002/pamm.201410320](https://doi.org/10.1002/pamm.201410320)
47. Phillips RJ, Armstrong RC, Brown RA, Graham AL, Abbott JR (1992) A constitutive equation for concentrated suspensions that accounts for shear-induced particle migration. *Phys Fluids A* 4(1):30–40. doi:[10.1063/1.858498](https://doi.org/10.1063/1.858498)
48. Ponte Castañeda P, Suquet P (2002) *Nonlinear composites and microstructure evolution*. Springer, Dordrecht
49. Schneider M (2015) Convergence of FFT-based homogenization for strongly heterogeneous media. *Math Methods Appl Sci* 38(13):2761–2778
50. Schneider M, Merkert D, Kabel M (2016) FFT-based homogenization for microstructures discretized by linear hexahedral elements. *Int’l J for Numerical Methods Eng* pp. 1–29
51. Schneider M, Ospald F, Kabel M (2016) Computational homogenization of elasticity on a staggered grid. *Int J Numer Methods Eng* 105(9):693–720
52. Schröder J (2014) A numerical two-scale homogenization scheme: the FE2-method, pp. 1–64. Springer Vienna, Vienna. doi:[10.1007/978-3-7091-1625-8\\_1](https://doi.org/10.1007/978-3-7091-1625-8_1)
53. Schröder J, Neff P (2003) Invariant formulation of hyperelastic transverse isotropy based on polyconvex free energy functions. *Int J Solids Struct* 40(2):401–445
54. Tyler DE (1987) Statistical analysis for the angular central Gaussian distribution on the sphere. *Biom Trust* 74(3):579–589
55. Voigt W (1889) Ueber die beziehung zwischen den beiden elasticitätsconstanten isotroper körper. *Annalen der Physik* 274(12):573–587
56. Vondřejc J, Zeman J, Marek I (2014) An FFT-based Galerkin method for homogenization of periodic media. *Comput Math Appl* 68:156–173



57. Widom B (1966) Random sequential addition of hard spheres to a volume. *J Chem Phys* 44(10):3888–3894
58. Yvonnet J, Monteiro E, He QC (2013) Computational homogenization method and reduced database model for hyperelastic heterogeneous structures. *Int J Multiscale Comput Eng* 11(3):201–225
59. Zheng QS, Du DX (2001) An explicit and universal applicable estimate for the effective properties of multiphase composites which accounts for inclusion distribution. *J Mech Phys* 49:2765–2788